

**Nonlinear Rosen-Zener-Stückelberg interferometry of a Bose-Einstein condensate**Sheng-Chang Li<sup>1,\*</sup> and Li-Bin Fu<sup>2</sup><sup>1</sup>*MOE Key Laboratory for Nonequilibrium Synthesis and Modulation of Condensed Matter, Shaanxi Province Key Laboratory of Quantum Information and Quantum Optoelectronic Devices, and School of Physics, Xi'an Jiaotong University, Xi'an 710049, China*<sup>2</sup>*Graduate School, China Academy of Engineering Physics, Beijing 100193, China*

(Received 22 March 2020; revised 24 August 2020; accepted 25 August 2020; published 8 September 2020)

We adopt a nonlinear two-mode model to investigate the Rosen-Zener-Stückelberg (RZS) interferometry of an interacting Bose-Einstein condensate trapped in double-well potential with a periodically modulating barrier. For symmetric potential, we analyze the properties of interference patterns and derive the interference conditions. For asymmetric potential, we explore the resonance structures caused by destructive interference at the weakly coupling limit and obtain the resonance conditions. In particular, we find that the chaotic motions in the asymmetric case with low-frequency modulation, can destroy the formation of interference fringes. In the symmetric case with high-frequency modulation, we see Fano-line-like resonance structures and find that the resonance positions exactly correspond to the boundary of macroscopic quantum self-trapping. We show that the nonlinearity can significantly alter both the shape and position of interference fringes and resonance structures. We discuss the experimental feasibility by comparing the solution of the Gross-Pitaevskii equation with both the solution of the two-mode model and the truncated Wigner simulation as well. The results suggest important applications of nonlinear RZS interferometry both in precisely controlling the dynamics and in accurately measuring the parameters of interacting many-body systems.

DOI: [10.1103/PhysRevA.102.033313](https://doi.org/10.1103/PhysRevA.102.033313)**I. INTRODUCTION**

The interacting Bose-Einstein condensate (BEC) trapped in double-well potential provides a representative quantum platform for the exploration of the physics of both macroscopic tunneling dynamics [1–4] and atomic matter-wave interference [5–10]. Due to the nonlinearity induced by the mean-field treatment of the interactions between coherent atoms, the system exhibits many remarkable dynamical phenomena that are distinguished from the traditional quantum systems, such as Josephson oscillations [11–13], self-trapping [14,15], nonlinear Landau-Zener tunneling [16–19] and Rosen-Zener (RZ) tunneling [20,21], and so on. The atomic interferometer [22] is a powerful tool for different measurements, ranging from probing the atomic properties [23], implementing the accurate measurements [24], to detecting the inertial effects [25]. The observation of BEC interference [26] brings a fascinating opportunity for investigating the properties of atomic matter-wave interferometry with BEC owing to its macroscopic coherence nature [27–29]. With the development of the techniques for manipulating ultracold atoms, a variety of interference schemes using trapped BEC have been proposed [5,30] and realized in experiments [31–36].

Considering the fundamental difference between optical and atomic interferometers caused by atom-atom interaction [9], the Mach-Zehnder [37–40], the Ramsey [41–44], the RZ [45], and the Landau-Zener-Stückelberg-Majorana

interferometries [16,17,46–49] have been extended to the nonlinear interaction cases because of the conceptual importance of these schemes. Recently, we proposed a Rosen-Zener-Stückelberg (RZS) interferometer [50] with double-well trapped interaction-free ultracold atoms and found some unique strengths compared to other interferometers. As a sequential work, in this paper, we mainly demonstrate the effects of atomic interactions on the RZS interference and resonance of BEC, because the interactions can be used to reduce phase diffusion [51–53], generate nonclassical correlations to improve the sensitivity [54,55], and create entanglement [56–62]. We study the influence of the symmetry of double-well potential and the modulation frequency of the barrier on the RZS interference and resonance under different strengths of atomic interactions. We find that the frequency shift and the shape deformation of both the interference fringes and the resonance constructions strongly depend on the strength of atomic interactions. We show that the chaotic motions in low-frequency modulation prevent the formation of interference fringes and the Fano-line-like resonance structure occurs at the self-trapping boundary with high-frequency modulation.

The paper is organized as follows. In Sec. II, we introduce the nonlinear two-mode RZ-train model. In Sec. III, we present the main results. The nonlinear RZS interference and resonance are categorized into two cases, i.e., low-frequency modulation and high-frequency modulation; in each case we, respectively, discuss the situations with symmetric and asymmetric potentials. In Sec. IV, we simulate the evolution of BEC based on the Gross-Pitaevskii (GP) equation and compare it with both the two-mode solution and the truncated Wigner simulation. Finally, we give a brief summary in Sec. V.

\*scli@xjtu.edu.cn

## II. NONLINEAR TWO-MODE RZ-TRAIN MODEL

We consider an atomic double-well BEC. Under the mean-field approximation, the dynamics of the system is governed by the GP equation  $i\hbar \frac{\partial \Psi(\mathbf{r}, t)}{\partial t} = [-\frac{\hbar^2 \nabla^2}{2m} + U(\mathbf{r}, t) + U_0 |\Psi(\mathbf{r}, t)|^2] \Psi(\mathbf{r}, t)$ , where  $U_0 = \frac{4\pi \hbar^2 a_s N}{m}$  describes the atomic interactions proportional to the  $s$ -wave scattering length  $a_s$ , and the total number  $N$  with  $m$  being the mass of atoms and  $U(\mathbf{r}, t)$  being the time-dependent double-well potential. For a sufficiently high barrier and weakly atomic interaction, one can describe the system by using a two-mode approximation (TMA) [55]. The two spatial modes localized in the left and right wells are given by the first spatially symmetric and first antisymmetric stationary eigenstates of the GP equation [12,14]. Under the TMA, the Hamiltonian of the system reads [21,43]

$$H(t) = \frac{V(t)}{2} \hat{\sigma}_x + \frac{\Delta + c(|b|^2 - |a|^2)}{2} \hat{\sigma}_z, \quad (1)$$

where  $a$  and  $b$  are the atomic population probabilities of the two spatial modes.  $\hat{\sigma}_{x,z}$  represent the Pauli matrices. The model Eq. (1) is fully characterized by three parameters: the energy bias  $\Delta$  between the two modes determined by the asymmetry of the double-well potential, the time-dependent coupling  $V(t) = V_0 + A \sin^2(\omega t) \geq 0$  (with amplitude  $A$ , frequency  $\omega$ , and offset  $V_0$ ) between the two modes inversely proportional to the height of the barrier, and the nonlinear interaction strength  $c$  describing the collision between the coherent atoms and can be flexibly changed by using the Feshbach resonances. The evolution of the system is controlled by the following nonlinear Schrödinger equation ( $\hbar = 1$ ),

$$i \frac{d}{dt} \mathbf{X}(t) = H(t) \mathbf{X}(t), \quad (2)$$

where  $\mathbf{X}(t) = [a(t), b(t)]^T$  is the two-component column vector. For convenience, we employ the adiabatic basis to describe the system, i.e.,  $\{|E(t)\rangle\}$ , which consists of the instantaneous eigenstates of the time-dependent Hamiltonian, i.e.,  $H(t)\mathbf{x}(t) = \mu(t)\mathbf{x}(t)$  with  $\mathbf{x}(t) = [\bar{a}(t), \bar{b}(t)]^T$ , where  $\mu$  is the chemical potential and is determined by the following algebraic equation:

$$(c + 2\mu)^2 [4\mu^2 - V(t)^2] - 4\Delta^2 \mu^2 = 0. \quad (3)$$

The eigenenergy  $E$  can be derived from the relation  $E = \mu - c(|\bar{a}|^4 + |\bar{b}|^4)/2$ . We illustrate the adiabatic energy levels (given by the values of  $\mu$ ) of the system with  $A = \omega = 1$  for both  $c = 0$  and  $c \neq 0$  in Fig. 1. In the linear case, i.e.,  $c = 0$ , it is clear that the energy gap between the two levels at the avoided crossings  $\omega t = n\pi$  (with integer  $n$ ) is equal to  $\sqrt{\Delta^2 + V_0^2}$ . However, in the nonlinear case, i.e.,  $c \neq 0$ , we see that the loop structures appear at the higher (or lower) energy level when  $c^2 > \Delta^2$  for  $V_0 = 0$  and  $\Delta \neq 0$  (see the green solid lines in Fig. 1), while the level crossings appear at the lower (or higher) energy level when  $c^2 > V_0^2$  for  $V_0 \neq 0$  and  $\Delta = 0$  (see the red broken lines in Fig. 1). The level-crossing points are located at  $\omega t = (2n+1)\pi/2 \pm \cos^{-1}[1 + 2(V_0 - c)/A]/2$  when  $c > 0$  and at  $\omega t = (2n+1)\pi/2 \pm \cos^{-1}[1 + 2(V_0 + c)/A]/2$  when  $c < 0$ . For the situations  $V_0\Delta = 0$ , the narrow energy gap at the avoided crossings is equal to  $V_0$

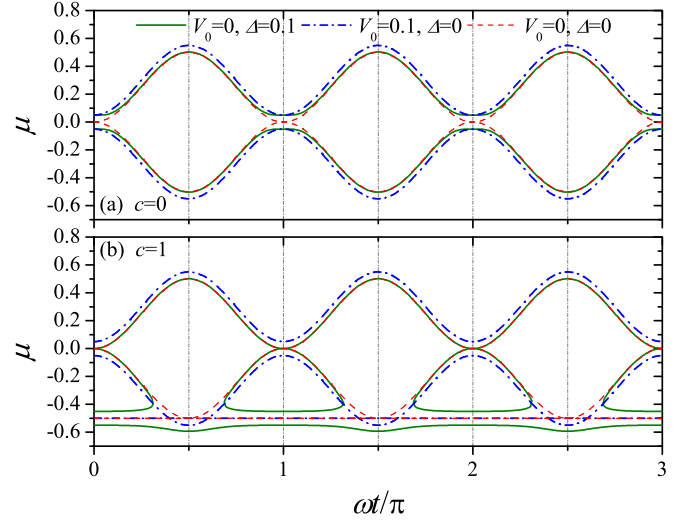


FIG. 1. Adiabatic energy levels with  $A = \omega = 1$  for (a) linear case  $c = 0$  and (b) nonlinear case  $c = 1$ . For the cases  $V_0\Delta = 0$ , the minimum energy gap at the avoided crossings is equal to  $V_0$  or  $|\Delta|$ . When  $V_0\Delta \neq 0$  and  $c^{2/3} > V_0^{2/3} + \Delta^{2/3}$  (not shown), the minimum level gaps at the avoided crossings are functions of  $\Delta$ ,  $V_0$ , and  $c$ .

or  $|\Delta|$  [see Fig. 1(b)]. For the situations  $V_0\Delta \neq 0$ , there are two, three, and four energy levels at the avoided crossings for  $c^{2/3} < V_0^{2/3} + \Delta^{2/3}$ ,  $c^{2/3} = V_0^{2/3} + \Delta^{2/3}$ , and  $c^{2/3} > V_0^{2/3} + \Delta^{2/3}$ , respectively, and the narrow energy gaps at the avoided crossings are functions of all three parameters ( $\Delta$ ,  $V_0$ ,  $c$ ). In the next section, we will explore the influence of the loop structure and the level crossing on the RZS interference and resonance, because in these level loop and crossing regions the number of the eigenvalues is more than two and thus the corresponding eigenstates are not orthogonal to each other.

## III. NONLINEAR RZS INTERFERENCE AND RESONANCE

Using the above two-mode atomic BEC system we are capable of realizing a nonlinear RZS interferometer, in which the nonlinearity is caused by the atomic interactions. The main structure of the interferometer based on the RZ-train model Eq. (1) is constructed by a sequence of RZ pulses of a sine-square form with the period  $T = \pi/\omega$ , which periodically modulates the coupling between the two modes. In our numerical experiments, initially, the BEC is prepared in one spatial mode, i.e.,  $[a(t=0), b(t=0)] = [0, 1]$ . When the RZ pulse turns on, the quantum tunneling between the two modes occurs. What we focus on is how does the periodic RZ-pulse field affect the population dynamics. Thus we record the populations of atoms in the other mode (i.e.,  $|a(t)|^2$ ) when the final RZ pulse turns off (i.e.,  $t = NT$  with  $N$  being the total number of the pulses) or at the end of each pulse (i.e.,  $t = nT$  with  $n = 1, 2, \dots$ ). The measurements are repeated with variable parameters either of the system (i.e.,  $\Delta$  and  $V_0$ ) or of the external field (i.e.,  $A$  and  $\omega$ ), and the RZS interference patterns are expected to build up in the parameter domain. In our simulations, we take the maximum strength of the periodic RZ-pulse field as the energy scale, namely,  $A = 1$ .

We begin our numerical simulations with  $V_0/A = 0$ , which means that, in the absence of periodic RZ-pulse field the

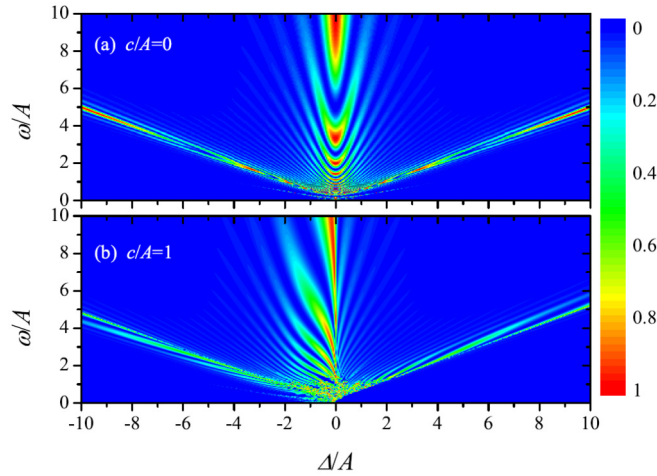


FIG. 2. RZS interference patterns shown by the final population probability (i.e.,  $|a(t = 20T)|^2$ ) distributions. For comparison, we give the results with  $V_0/A = 0$  both for (a)  $c/A = 0$  and for (b)  $c/A = 1$ .

barrier is so high that the BEC in the two spacial modes are decoupled. In Fig. 2, we show the RZS interference patterns formed by evolving the system from  $t = 0$  to  $t = 20T$ . We see that the interference fringes can be destructive or constructive, which are determined by the relative phase (between two modes) acquired during the evolution. In the linear case [see Fig. 2(a)], the interference pattern is of axial symmetry structure and the main distribution of  $|a(t = 20T)|^2$  is symmetrically centered on three lines denoted by  $\omega/\Delta = \infty, \pm 1/2$ , respectively. For the simplest case  $c = \Delta = V_0 = 0$  [corresponding to the line  $\Delta/A = 0$  in Fig. 2(a)], the analytical solution for  $|a(t = NT)|^2$  can be expressed as  $\sin^2[A(2N\pi - \sin[2N\pi])]/(8\omega)$ . However, in the nonlinear case [see Fig. 2(b)], the axial symmetry of the interference pattern is severely damaged. This implies that the nonlinearity induced by the atomic interactions can strongly modify the features of the RZS interferometry. Subsequently, we divide the study into two cases by comparing the modulation frequency  $\omega$  with the modulation amplitude  $A$  to explore the effects of the nonlinearity on the properties of RZS interference and resonance. For each case we focus on two main situations, namely,  $\Delta/A = 0$  and  $V_0/A = 0$ .

### A. Low-frequency modulation

When the modulation frequency  $\omega$  is comparable to, or smaller than the modulation strength  $A$  and the interaction strength  $c$ , we label it as the low-frequency modulation case. For example, the regime  $\omega/A \leq 1$  in Fig. 2(b), where we see the emergence of chaos in small  $|\Delta|/A$  regions. In Fig. 3, we plot the final population probability  $|a(t = 2T)|^2$  as a function of  $V_0/A$  and  $\Delta/A$  for different values of  $c/A$  with  $\omega = 1$ . In Fig. 3(a),  $\Delta/A = 0$ , it is found that the dependence of the interference fringes in the  $V_0/A$  domain on the nonlinear parameter  $c/A$  in large  $V_0/A$  (e.g.,  $> 3$ ) region is rather weak, and the fringes for small nonlinearity (e.g.,  $|c/A| < 1.5$ ) show a regular oscillation [see Fig. 3(c)]. For the case  $\Delta = c = 0$ , the analytical solution of the Schrödinger Eq. (2) reads

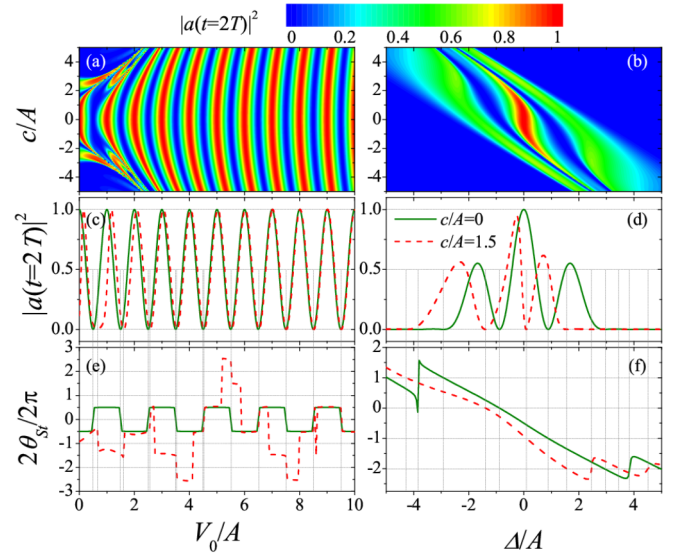


FIG. 3. Nonlinear RZS interference patterns with low-frequency modulation given by the final population probability  $|a(t = 2T)|^2$  for (a)  $\Delta/A = 0$  and (b)  $V_0/A = 0$ . (c) and (d) The corresponding profiles of  $c/A = 0$  and  $c/A = 1.5$ . (e) and (f) The corresponding rescaled Stückelberg phase  $2\theta_{St}/2\pi$ . The parameters are  $A = \omega = 1$ .

$|a(t)|^2 = \sin^2[(A + 2V_0)t/4 - (A \sin[2\omega t])/(8\omega)]$ . When  $t = 2T$ , the fringes in the  $V_0$  domain can be described by the function  $\sin^2[(A + 2V_0)\pi/2]$  with a period 1, which are in good agreement with the numerical results shown in Fig. 3(c). In Fig. 3(b),  $V_0/A = 0$ , we see that  $|a(t = 2T)|^2$  is small in the entire regime for  $c\Delta > 0$  and the fringes in the  $\Delta/A$  domain mainly distribute in the regions  $(\pm 3.2 - c/A)$  for a given  $c/A$ . Moreover, in this case, we find that the nonlinearity can lead to severe compression and displacement of the fringes [see Fig. 3(d)].

To find the conditions of the RZS interference in the low-frequency modulation regime, for simplicity, here we map the nonlinear RZ-train model Eq. (1) to a classical Hamiltonian. According to Refs. [19,43], we introduce  $\theta = \arg b - \arg a$  and  $s = |b|^2 - |a|^2$  as canonical variables, which denote the relative phase and the population imbalance between the two modes, respectively. As a result, we obtain the classical Hamiltonian as follows:

$$\mathcal{H} = -\left(\Delta + \frac{c}{2}s\right)s + V(t)\sqrt{1 - s^2} \cos \theta. \quad (4)$$

We define the relative phase accumulated in one periodic evolution as the Stückelberg phase, namely,  $\theta_{St} \equiv \theta(T) - \theta(0) = \int_0^T (\partial\mathcal{H}/\partial s) dt$ . In our case,  $\theta(0) = 0$ , and thus  $\theta_{St} \equiv \theta(T)$ . In Figs. 3(e) and 3(f), we have demonstrated the rescaled Stückelberg phase  $\theta_{St}/\pi$  as a function of  $V_0/A$  and  $\Delta/A$ . Both for the linear and nonlinear cases, we see that the minimum values of  $|a(t = 2T)|^2$  are located at  $2\theta_{St} = 2n\pi$  while the maximum values are located at  $2\theta_{St} = (2n + 1)\pi$  with  $n = 0, \pm 1, \pm 2, \dots$ . Similarly, the conditions of the constructive and destructive interferences for  $N$ -period evolution are given by

$$N\theta_{St} = (2n + 1)\pi \quad \text{and} \quad N\theta_{St} = 2n\pi, \quad (5)$$

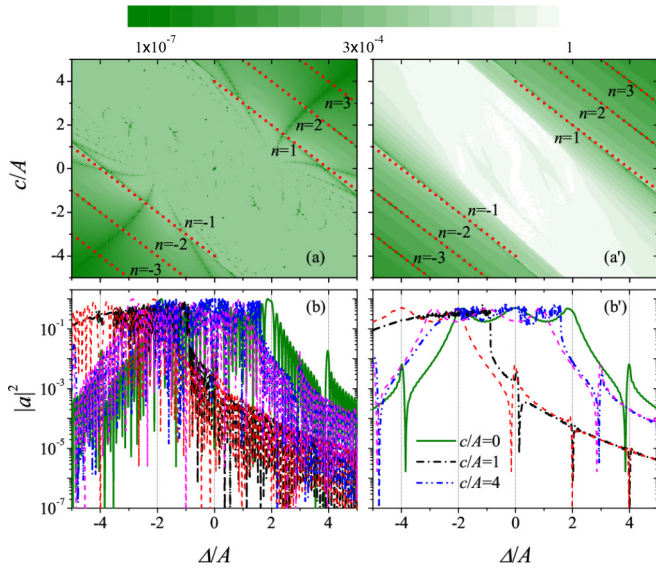


FIG. 4. Nonlinear RZS resonance structures with low-frequency modulation for (a) final population probability  $|a(t = 20T)|^2$  and (a') periodic-averaged population probability  $\frac{1}{20} \sum_{l=1}^{20} |a(t = lT)|^2$ . Red dotted lines demonstrate the results determined by  $\Theta_{St} = 2n\pi$  with  $n = \pm 1, \pm 2, \dots$  (b) and (b') The corresponding profiles of  $c/A = 0, 1, \text{ and } 4$ . Thick solid, dash-dot, and dash-dot-dot lines denote the exact solutions obtained from Eq. (2) while thin broken red lines denote the approximate solution given by Eq. (6) for comparison. The parameters are  $A = \omega = 1$  and  $V_0/A = 0$ .

respectively. These conditions imply that, for a given initial state, the nonlinear RZS interference characterized by the final population probability in one mode is only determined by the relative phase between the two modes accumulated during the first RZ pulse. It must be mentioned that, with the increase of the number of evolution cycles, the RZS interference fringes given by the final population probability will become more and more dense. Alternatively, it would be a better way to measure the population probability at the end of each cycle and then average them as the interference signal. Actually, the averaging operation can result in the disappearance of many interference fringes obtained from the ultimate measurements. To show this effect, we calculate the periodic-averaged occupation probability, i.e.,  $\frac{1}{N} \sum_{l=1}^N |a(t = lT)|^2$ . The numerical results with  $\omega = 1$  and  $N = 20$  for different nonlinear interactions are illustrated in Figs. 4(a') and 4(b'). As a comparison, we also show the corresponding results for the final population probability in Figs. 4(a) and 4(b). In these cases, the population probabilities for  $|a|^2$  are very small. To clearly see the resonance structures corresponding to the destructive interference, we have employed logarithmic coordinates.

For the weak-coupling limit case,  $V_0/A \rightarrow 0$ , the tunneling between the two modes is weak enough and thus we can use the approximations  $|a(t)|^2 \simeq |a(t = T)|^2$  and  $|b(t)|^2 \simeq |b(t = T)|^2$ . Under this condition, one can transform the RZ-train model from the Schrödinger picture to the Dirac picture by introducing the gauge transformation  $\mathbf{X}(t) = U(t)\mathbf{X}'(t)$  with  $U(t) = \exp[-i(\frac{\Delta}{2}t + \frac{c}{2}[|b(t = T)|^2 - |a(t = T)|^2]t)\hat{\sigma}_z]$ , where  $\mathbf{X}'(t) = [a'(t), b'(t)]^T$  is the new two-component vector with the same probability as the old

one. In the new basis, Eq. (2) becomes

$$i\frac{d}{dt}\mathbf{X}'(t) = \begin{pmatrix} 0 & \Omega \\ \Omega^* & 0 \end{pmatrix}\mathbf{X}'(t), \quad (6)$$

with

$$\Omega = \frac{V(t)}{2}e^{i\Theta(t)}, \quad \Theta(t) = [\Delta + cs(t = T)]t, \quad (7)$$

where  $\Omega$  denotes the effective Rabi frequency measuring the coupling between the two modes with  $s(t = T) = |b(T)|^2 - |a(T)|^2$ . The symbol  $*$  indicates the complex conjugate. For one cycle evolution, the argument of the effective coupling parameter, namely,  $\Theta \pm 2\omega t$ , can be approximate to  $\Theta_{St} \simeq T[\Delta + cs(t = T) \pm 2\omega]$ . For convenience, we label  $\Theta_{St}$  as the Stokes phase, which determines the positions of the resonance caused by the destructive RZS interference. Accordingly, for the  $N$ -cycle evolution the condition of the resonances can be obtained by minimizing the effective coupling, which is

$$\Theta_{St} = 2n\pi \text{ or } [\Delta + cs(t = T)] = 2(n \pm 1)\omega, \quad (8)$$

where  $n$  are positive and negative integers for  $\pm$ , respectively. In Figs. 4(a) and 4(a'), we have shown the resonance positions by the red dotted lines given by Eq. (8). It is found that, for larger  $c\Delta$  (i.e., larger  $|n|$ ), e.g., when  $n = \pm 3$ , the above Eq. (8) can accurately predict the resonance positions for both final-population and periodic-averaged-population signals. In fact, at the weak-coupling limit, the tunneling probability is small enough and can be safely neglected, therefore, the initial condition  $s(t = 0) = 1$  gives a good approximation of  $s(t = T)$  and then Eq. (6) reduces to a linear model. Based on this linear model, we have calculated the final and the periodic-averaged probabilities of  $|a'|^2$  and compared with the exact solutions obtained by directly solving the nonlinear Schrödinger Eq. (2). From Fig. 4(c) we find that the two results for the periodic-averaged measurement are in good agreement when  $c\Delta$  is larger or  $n \geq 2$ . Particularly, we see some random oscillations in the region  $\Delta/A \in (-2.4, 1.6)$  for  $c/A = 1$ , which imply the emergence of Hamiltonian chaos. To confirm this, we show the typical behavior of the Poincaré section (obtained by stroboscopic plotting of the classical trajectories with period  $T$ ) of  $\mathcal{H}(t)$  in Fig. 5 for  $c/A = 1$  and  $V_0/A = 0$  with the parameter  $\Delta/A$  ranging from 0.471 to 3.471. It is clear that, for small values (i.e.,  $< 1.6$ ) of  $\Delta/A$ , the phase space is dominated by chaotic motions [see Figs. 5(a) and 5(b)], whereas for large values (i.e.,  $> 1.6$ ) of  $\Delta/A$ , the dynamics is primarily regular [see Figs. 5(c) and 5(d)]. It is important to emphasize that, by introducing the time-dependent periodic modulation into the nonlinear two-mode model, the degrees of freedom for the system are increased from two to three and thus the minimum dimensions permitting the chaotic behaviors are satisfied.

## B. High-frequency modulation

When the modulation frequency  $\omega$  is much larger than the modulation amplitude  $A$  and the nonlinearity  $c$ , we refer to it as the high-frequency modulation case. In this case, we also study two typical situations as mentioned previously. First, we analyze the situation for  $\Delta/A = 0$ . To meet the

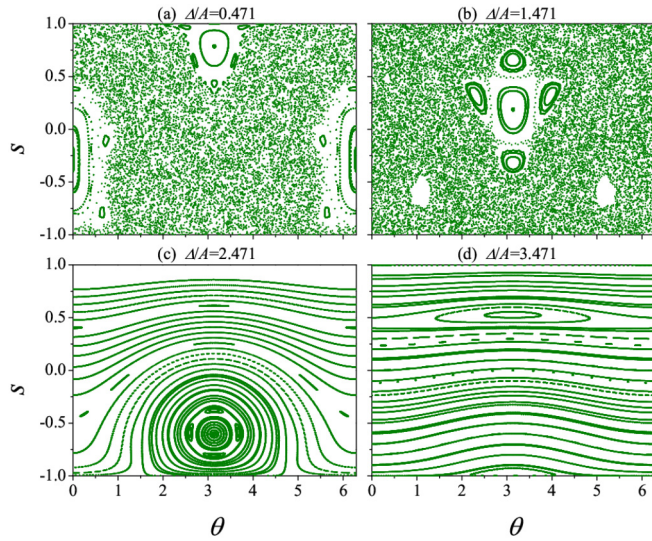


FIG. 5. Poincaré sections of the Hamiltonian system (4) for  $V(t) = V_0 + A \sin^2(\omega t)$  with  $\omega = 1$  and  $V_0 = 0$ , obtained by stroboscopic plotting of the trajectories with period  $T = \pi/\omega$  for different energy biases: (a)  $\Delta/A = 0.471$ , (b)  $\Delta/A = 1.471$ , (c)  $\Delta/A = 2.471$ , and (d)  $\Delta/A = 3.471$ .

condition for the high-frequency modulation, in the simulations we set  $\omega = 100$ . For different nonlinear interaction strengths, we obtain the RZS reference fringes in  $V_0/A$  domain and demonstrate them in Fig. 6(a). Here we take the final population probability as the interference signature. It is easy to see that the effect of nonlinearity on the interference pattern is not significant if  $V_0/A$  is not small. In the simplest

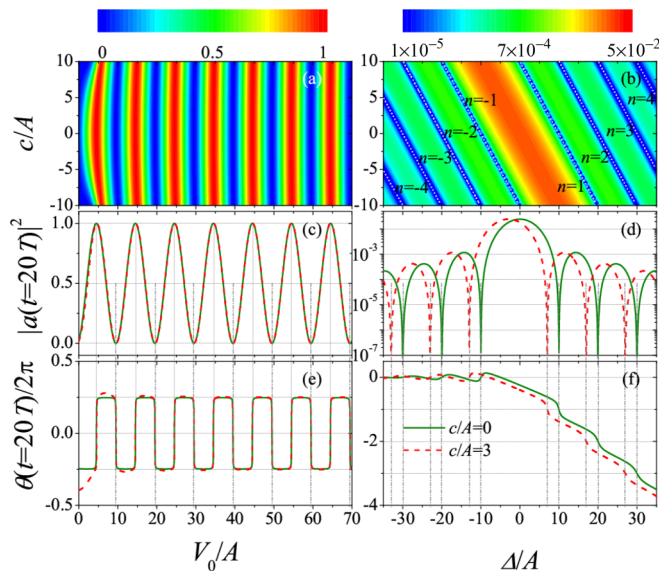


FIG. 6. Nonlinear RZS interference patterns of  $|a(t = 20T)|^2$  with high-frequency modulation for (a)  $\Delta/A = 0$  and (b)  $V_0/A = 0$ . The profiles for  $c/A = 0$  (olive solid lines) and  $c/A = 3$  (red dotted lines) illustrate in (c) for  $\Delta/A = 0$  and in (d) for  $V_0/A = 0$ . (e) and (f) The rescaled final relative phase  $\theta(t = 20T)$  corresponding to (c) and (d). We mark the resonance positions by white dotted lines given by Eq. (13). The parameters are  $A = 1$  and  $\omega = 100$ .

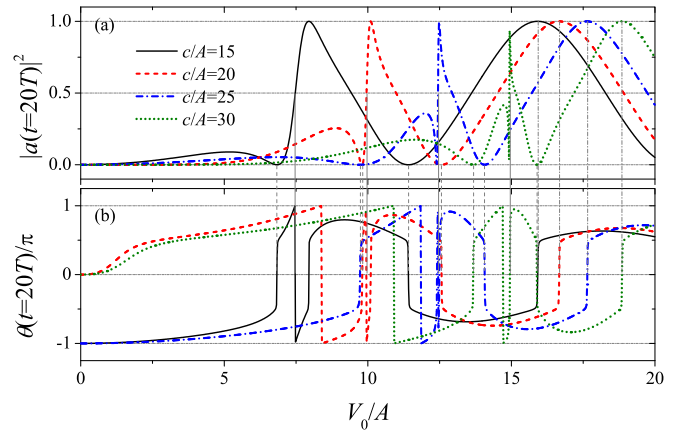


FIG. 7. Fano-line-like resonance structures for different nonlinear strengths with high-frequency modulation. (a) and (b) The final population probability  $|a(t = 20T)|^2$  and the final relative phase  $\theta(t = 20T)$ , respectively. The vertical gray solid, dashed, and dash-dotted lines mark the positions of Fano-line-like resonance, destructive interference, and constructive interference, respectively. The parameters are  $\Delta = 0$ ,  $A = 1$ , and  $\omega = 100$ .

linear case, i.e.,  $\Delta = c = 0$ , we can derive the analytical solution of the Schrödinger Eq. (2); it is  $|a(t)|^2 = \sin^2[(A + 2V_0)t/4 - (A \sin[2\omega t])/(8\omega)]$ . For  $t = 20T$ , the interference fringes in the  $V_0$  domain are well described by the function  $\sin^2[(A + 2V_0)\pi/20]$  with the period being 10, which are in good agreement with our numerical results shown in Fig. 6(c). As a result, for  $N$  period evolution, the conditions for the constructive and destructive interferences, respectively, read

$$NV_0 = (2n + 1)\omega \quad \text{and} \quad NV_0 = 2n\omega, \quad (9)$$

with  $n = 0, 1, 2, \dots$ . In the weakly nonlinear case, i.e.,  $|c| < 2V_0$ , the coupling between the two modes is strong and the tunneling between them leads to a Rabi-type oscillation of the final population  $|a(t = NT)|^2$  with  $V_0$  [see Fig. 6(c)]. Correspondingly, the final relative phase  $\theta(t = NT)$  also illustrates a synchronous oscillation [see Fig. 6(e)] limited in a narrow range  $(-\pi, \pi)$  and thus the interference conditions cannot be expressed as those in the low-frequency modulation case by Eq. (5). Alternatively, here we employ the final relative phase between the two modes to give the interference conditions, i.e.,

$$\theta(t = NT) = 0 \quad \text{and} \quad \begin{cases} \frac{d\theta(t=NT)}{dV_0} > 0, & \text{constructive;} \\ \frac{d\theta(t=NT)}{dV_0} < 0, & \text{destructive.} \end{cases} \quad (10)$$

We find that this final relative phase criterion for the nonlinear RZS interference with high-frequency modulation still works well in the linear case. In the strongly nonlinear case, i.e.,  $|c| > 2V_0$ , the tunneling between the two modes is very small due to the appearance of loop structure at energy levels. This regime is often called the macroscopic self-trapping phase. In this region we find that the conditions for interference are just the opposite of those for the weak nonlinearity, i.e.,  $d\theta(t = NT)/dV_0 < 0$  and  $d\theta(t = NT)/dV_0 > 0$  for the constructive and destructive interferences, respectively. For instance, in Fig. 7, we have shown the situations for both weakly and

strongly nonlinear cases, which support the interference conditions we have given above. It should be mentioned that, in some cases, the final relative phase between the two modes can go out of the range  $[-\pi, \pi]$  but we have still limited it to this range because of the periodicity of  $\theta$ . In particular, at the boundary between the strong and weak nonlinearities, i.e.,  $|c| = 2V_0$ , we see the obvious Fano-line-like resonance structures [see Fig. 7(a)]. Moreover, we find that the stronger the nonlinearity, the narrower the resonance width.

Now we discuss the situation for  $V_0 = 0$  in the high-frequency modulation case. In this limit case, the coupling between the two modes is small enough and can be safely neglected in most situations. Similar to the plot in the low-frequency modulation case, here we adopt the logarithmic coordinates demonstrating the exact results obtained from Eq. (2) for different nonlinearities in Fig. 6(b). A parallel diagonal pattern for interference has been seen. To find the resonance (refer to the destructive interference) condition, we also calculate the final relative phase shown in Fig. 6(f) corresponding to the resonances illustrated in Fig. 6(d). Accordingly, we obtain the condition of resonance as follows:

$$\theta(t = NT) = 2n\pi \text{ and } \begin{cases} \frac{d\theta(t=NT)}{d\Delta} > 0, & \Delta < 0; \\ \frac{d\theta(t=NT)}{d\Delta} < 0, & \Delta > 0; \end{cases} \quad (11)$$

with  $n = 0, \pm 1, \pm 2, \dots$ . This condition also can apply to both linear and nonlinear cases [see Fig. 6(f)]. Finally, we try to give some approximate results from Eq. (6). In this high-frequency modulation case, the effective coupling is characterized by the Rabi frequency,

$$\Omega \simeq \frac{A}{4} e^{i\theta}. \quad (12)$$

In this expression, we have neglected the high-frequency oscillation terms  $-\frac{A}{8} e^{i[\theta(t) \pm 2\omega t]}$ . For one cycle evolution, the argument of the effective coupling parameter  $\Theta(t)$  gives the Stokes phase, which can be approximate to  $\Theta_{St} \simeq T[\Delta + cs(t = T)]$  and determines the positions of the resonance caused by the destructive interference. Similarly, for  $N$ -cycle evolution, the condition of the resonances is given by minimizing the effective coupling, which requires

$$N\Theta_{St} = 2n\pi \text{ or } N[\Delta + cs(t = T)] = n\omega, \quad (13)$$

where  $n = \pm 1, \pm 2, \dots$ . In Fig. 6(b), we have marked the resonance positions by the white dotted lines given by the above Eq. (13). It is seen that Eq. (13) can accurately predict the resonance positions for both linear and nonlinear cases. Actually, at the weak-coupling limit, we can use  $s(t = T) \simeq s(t = 0) = 1$  and then the resonance condition in Eq. (13) can be simplified to  $N(\Delta + c) = n\omega$ . Using the above approximation, we have calculated the final probability and the periodic-averaged probability of  $|a|^2$  from Eq. (6) and compared with the exact solutions obtained by directly solving the nonlinear Schrödinger Eq. (2). From Fig. 8(a) we find that the results for both two outputs are in good agreement. For the final measurements, our two different conditions Eqs. (11) and (13) for the resonances work well. We emphasize that the periodic-averaged outputs and the corresponding Stückelberg phase criterion [see the red dash-dotted line in Fig. 8(b)] used

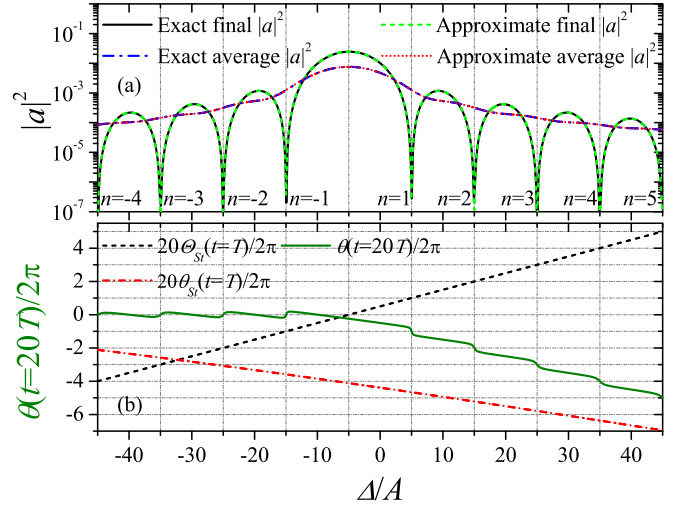


FIG. 8. (a) Nonlinear RZS resonances with high-frequency modulation for  $V_0/A = 0$  and  $c/A = 5$  of final population probability  $|a(t = 20T)|^2$  and periodic-averaged population probability  $\frac{1}{20} \sum_{t=1}^{20} |a(t = IT)|^2$ . The corresponding approximate solutions obtained from Eq. (6) have also been shown for comparison. (b) Three rescaled relative phases, i.e., the final relative phase  $\theta(t = 20T)$ , the 20 times of the Stückelberg phase  $\theta_{St}$ , and the 20 times of the Stokes phase  $\Theta_{St}$ , shown as the functions of  $\Delta/A$ . The parameters are  $A = 1$  and  $\omega = 100$ .

in the low-frequency modulation cases cannot give any useful information when they apply to the high-frequency modulation cases.

#### IV. EXPERIMENTAL FEASIBILITY ANALYSIS

In this section, we try to connect the above theoretical analysis to the actual BEC experiment [9,10]. To this end, we need to simulate the evolution of condensate by solving the time-dependent GP equation. The dimensionless version of the one-dimensional GP equation reads ( $\hbar = m = 1$ )

$$i \frac{\partial \psi}{\partial t} = \left[ -\frac{1}{2} \frac{\partial^2}{\partial x^2} + V_{dw}(x, t) + g_0 |\psi|^2 \right] \psi, \quad (14)$$

where the double-well potential  $V_{dw}$  takes the form of

$$V_{dw}(x, t) = \frac{1}{2} x^2 + V_b(t) e^{-x^2/(2w^2)} + f x. \quad (15)$$

The periodically modulated barrier height, the separation of two wells, and the tilt of the potential are, respectively, characterized by  $V_b(t) = V_i - A \sin^2(\omega t)$ ,  $w$ , and  $f$ . In the description of Eqs. (14) and (15), the distances, time, and energies have been scaled by  $\sqrt{\hbar/(m\omega_x)}$  (with  $\omega_x$  being the harmonic frequency),  $1/\omega_x$ , and  $\hbar\omega_x$ , respectively.

Using the TMA, the wave function can be expressed as [12,14]  $\psi(x, t) = \psi_L(t)\Phi_L(x) + \psi_R(t)\Phi_R(x)$ . The two modes are described by the spatial wave functions  $\Phi_{L,R} = (\Phi_e \pm \Phi_g)/\sqrt{2}$ , where  $\Phi_g$  and  $\Phi_e$  are the instantaneous ground and first-excited states of the stationary GP equation, i.e.,  $[-\frac{1}{2} \frac{\partial^2}{\partial x^2} + V_{dw}(x) + g_0 |\Phi_{g,e}|^2] \Phi_{g,e}(x) = E_{g,e} \Phi_{g,e}(x)$ . The orthogonality condition and the normalized condition are  $\int \Phi_i \Phi_j dx = \delta_{i,j}$  (with  $i, j = L, R$ ) and  $|\psi_L|^2 + |\psi_R|^2 = 1$ . As

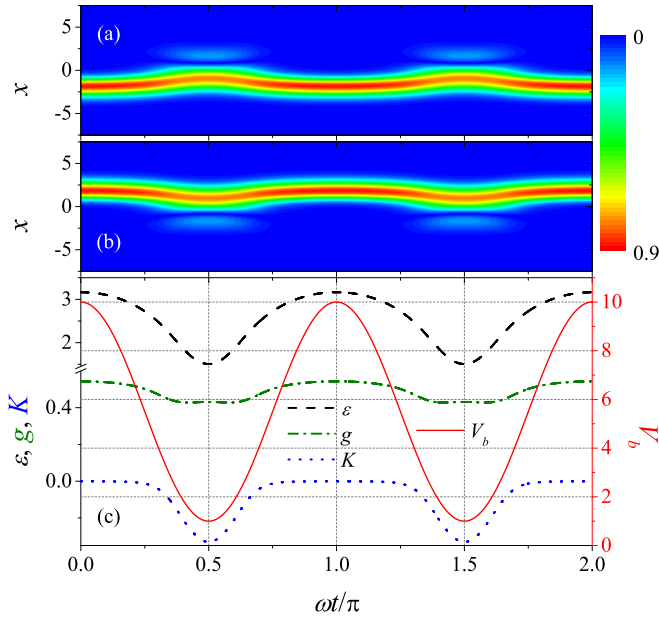


FIG. 9. Wave-function distribution of the two spatial modes: (a)  $|\Phi_L|$  and (b)  $|\Phi_R|$ . (c) Variation of both the parameters in the two-mode Schrödinger equation and the height of the barrier between two wells over time. We have set  $V_i = 10$ ,  $A = 9$ ,  $w = 1/\sqrt{2}$ , and  $g_0 = 1$ .

a result, we obtain the two-mode Schrödinger equation to govern the dynamics of a weakly coupled BEC as follows:

$$i \frac{d}{dt} \mathbf{Y}(t) = \begin{pmatrix} \epsilon_L + g_L |\psi_L|^2 & K \\ K & \epsilon_R + g_R |\psi_R|^2 \end{pmatrix} \mathbf{Y}(t), \quad (16)$$

where  $\mathbf{Y}(t) = [\psi_L(t), \psi_R(t)]^T$ .  $\epsilon_i = \int [\frac{1}{2} |\nabla \Phi_i|^2 + V_{dw}(x) |\Phi_i|^2] dx$  (with  $i = L, R$ ),  $g_i = g_0 \int |\Phi_i|^4 dx$ , and  $K = \int [\frac{1}{2} \nabla \Phi_L \nabla \Phi_R + \Phi_L V_{dw}(x) \Phi_R] dx$ . For convenience, in the following simulation we focus on the symmetric double-well potential [10], i.e.,  $f = 0$ . In this case the parameters in Eq. (16) are simplified to  $\epsilon_{L,R} = \epsilon$  and  $g_{L,R} = g$ . We select the parameters as  $V_i = 10$ ,  $w = 1/\sqrt{2}$ ,  $A = 9$ , and  $g_0 = 1$ . The results for the wave functions of two modes with different heights of the barrier are shown in Figs. 9(a) and 9(b). The coefficients of the two-mode equation are demonstrated in Fig. 9(c) as well.

To simulate the evolution of condensate and verify the validity of TMA, we directly solve the time-dependent GP equation (14) by employing the operator-splitting method. Initially, the barrier is very high and the atoms are prepared in the right well, i.e.,  $|\psi_R(0)|^2 = 1$ . To prevent the atoms from being excited into higher excited states, the height of the barrier must adiabatically vary. According to Ref. [50], the adiabatic condition for the parameters we selected is  $\omega \ll 0.8306$  or  $T \gg 3.7823$ . The final probability of the atoms occupying in the left well  $P_L$  is sensitive to  $\omega$ . In the top panel of Fig. 10, we show three typical tunneling behaviors of condensate evolving two cycles: (i) Atoms dominate the right well [see Fig. 10(a)]; (ii) atoms dominate the left well [see Fig. 10(b)]; (iii) atoms occupy both wells alternately [see Fig. 10(c)]. Taking periodic-averaged measurement, i.e.,  $\bar{P}_L = \frac{1}{T} \sum P_L(t = lT)$ ,

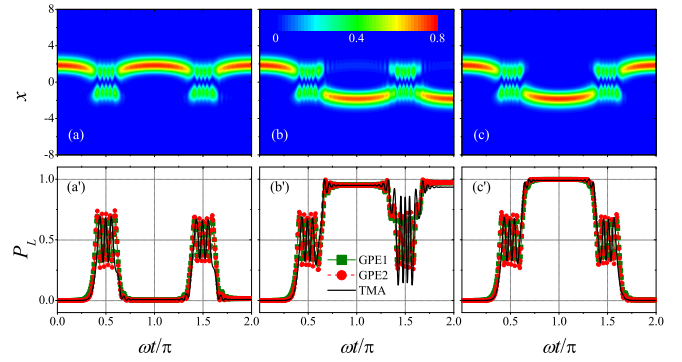


FIG. 10. (Top panel) Time evolution of the population probability  $|\psi|^2$  for different modulation periods. (Bottom panel) Comparison between the solution of the GP equation and the TMA result for the population probability of atoms in the left well. GPE1 denotes the probability of atomic population left of the barrier while GPE2 illustrates the probability given by the projection measurement. (a) and (a')  $T = 287$ , (b) and (b')  $T = 309.5$ , and (c) and (c')  $T = 319$ . We have set  $V_i = 10$ ,  $A = 9$ ,  $w = 1/\sqrt{2}$ , and  $g_0 = 1$ .

the first two cases correspond to the destructive interference and constructive interference, respectively. For comparison, we also illustrate the solutions obtained from the two-mode equation (16) in the bottom panel of Fig. 10. We calculate two experimental observables:  $\int_{-\infty}^0 |\psi(x)|^2 dx$  (GPE1 in Fig. 10) and  $|\int_{-\infty}^{+\infty} \psi^*(x) \Phi_L(x) dx|^2$  (GPE2 in Fig. 10). We find that these two quantities are in good agreement with each other. Moreover, we see that the consistency between the solutions of the GP equation and TMA is also good in most time evolution regions. However, in the Josephson oscillation regions around  $\omega t/\pi = (2n+1)/2$  (with  $n = 0, 1, \dots$ ), there is a slight inconsistency between the two solutions, because in these regions the barrier is so low that TMA does not hold [i.e., the two modes cannot be completely localized and spatially separated as shown in Figs. 9(a) and 9(b)].

Now we discuss the validity of the mean-field approximation presented above. We know that the mean-field GP equation describes the dynamics of a weakly interacting atomic condensate at zero temperature when  $N \rightarrow \infty$ . It does not consider the effects of thermal noise and quantum noise. However, a real-world BEC made of ultracold atoms suffers from depletion in the course of its time evolution and this may affect the double-well dynamics of the condensate. Here we make a quantitative analysis of the impact of effects beyond the mean-field approximation via the truncated Wigner (TW) calculations [63]. The basic idea of the TW method is that one can map a problem in quantum phase space (using the Wigner function) to a set of stochastic differential equations [64]. According to Ref. [63], the stochastic GP equation for our problem with two-body dissipation terms reads

$$i \frac{\partial \psi}{\partial t} = \left[ -\frac{1}{2} \frac{\partial^2}{\partial x^2} + V_{dw} + (g_0 - i\kappa) |\psi|^2 + i\sqrt{\kappa} \xi \right] \psi, \quad (17)$$

where  $\kappa$  is the dissipation parameter describing the local two-body collisional losses [63] and can be approximated by  $\sqrt{\kappa} \simeq \frac{12ma_z^2 k T_{NC}}{\pi \hbar^2}$  with  $k$  being Boltzmann's constant and  $T_{NC}$  being the temperature of the noncondensate

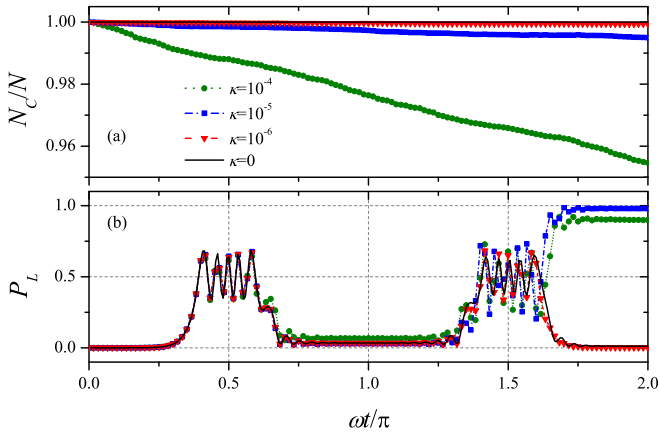


FIG. 11. (a) TW calculations for the time evolution of the total atomic number of condensate for different dissipation parameters  $\kappa$ . (b) Corresponding results for the population probability of atoms in the left well. For comparison, we also show the results from GP equation simulations (i.e.,  $\kappa = 0$ , solid black lines). We have set  $V_i = 10$ ,  $A = 9$ ,  $w = 1/\sqrt{2}$ ,  $T = 300$ ,  $N = 10^5$ ,  $M = 128$ ,  $\Delta x = 0.125$ , and  $g_0 = 1$ .

[65].  $\xi(x, t)$  is a complex stochastic  $\delta$ -correlated Gaussian noise with  $\langle \xi(x, t) \xi^*(x', t') \rangle = \delta(x - x') \delta(t - t')$ . For the initial condition  $\psi(0) = \Phi_R(x) + \eta(x)$  with  $\eta(x) = [\eta_r(x) + i\eta_i(x)]/2\sqrt{N\Delta x}$  (where  $\Delta x$  is the grid spacing;  $\eta_r$  and  $\eta_i$  are two independent Gaussian random numbers with mean 0 and standard deviation 1 at each grid point), we do many simulations based on Eq. (17) each with different noise and then we can estimate the atomic number of condensate by  $N_C = N[\sum_{j=1}^M |\psi(x_j)|^2 \Delta x - \frac{M}{2N}]$  (with  $M$  being the total number of grid points; refer to Ref. [64] for more details). In Fig. 11, we demonstrate our TW calculations for the time evolution of the proportion of condensate [see Fig. 11(a)] and the population probability of atoms in the left well [see Fig. 11(b)]. For the case with small dissipation (e.g.,  $\kappa = 10^{-6}$ ), we see that the TW calculation is consistent with the GP equation simulation during whole two cycles. For the condensate of  $^{87}\text{Rb}$  atoms with  $a_s \simeq 100a_0$  (where  $a_0$  is the Bohr radius), the value  $\kappa = 10^{-5}$  corresponds to a temperature approximately  $T_{\text{NC}} \simeq 168\text{nK}$  at which the deviations from the GP calculations become visible at finite time scales. Actually, the final population probability  $P_L$  mainly depends on the dynamics of the Josephson oscillation stage of the evolution process. Fortunately, it is shown that the experimental results are in good agreement with the GP equation simulations during this period [66].

Finally, it must be mentioned that for the atomic BEC, the atom-atom interaction can be controlled by the Feshbach

resonance technique, the double-well potential (15) can be formed by superimposing a blue-detuned laser beam upon the center of a magnetic trap and the barrier height can be adjusted by changing the intensity of the blue-detuned laser beam [26], and the tilt of the potential can be achieved through a magnetic field, a gravity field, or a light shift [67]. One can also use the rf dressing technique [68,69] to realize the double-well potential with tunable barrier height and tilt. Therefore, the nonlinear RZS interference and resonance based on the double-well BEC can be observed under current experimental conditions [9,10,66].

## V. CONCLUSION

In conclusion, we have investigated the nonlinear RZS interferometry of double-well BEC based on the two-mode RZ-train model and demonstrated that both the coherent atomic interactions and the periodic RZ-pulse field can strongly affect the properties of the interference. For the symmetric potential case, we have analyzed the features of RZS interference patterns and derived the interference condition. For the asymmetric potential case, we have explored the resonance structures caused by the destructive interference at the weakly coupling limit and obtained the resonance condition. Particularly, it is found that the chaotic motions in the asymmetric case with low-frequency modulation, can destroy the formation of interference fringes. In the symmetric case with high-frequency modulation, the structures of Fano-line-like resonance have been shown and the resonance positions are found to exactly be the boundary of the macroscopic quantum self-trapping. We have also analyzed the experimental feasibility by comparing the solution of the GP equation with both the TMA solution and the TW calculation. The sensitivity of interference fringes and resonance structures to both system parameters and periodic pulse field suggests important applications of our nonlinear RZS interferometry in precisely controlling the dynamics and in accurately measuring the parameters of interacting many-body systems.

## ACKNOWLEDGMENTS

We thank A. Smerzi and S. P. Nolan for their useful discussions during the manuscript revision stage. This work is supported by the National Natural Science Foundation of China (Grants No. 11974273, No. 11725417, and No. U1930403), the Science Challenge Project (Grant No. TZ2018005), and the Natural Science Fundamental Research Program of Shaanxi Province of China (Grant No. 2019JM-004).

- [1] F. Dalfovo, L. Pitaevskii, and S. Stringari, *Phys. Rev. A* **54**, 4213 (1996).  
 [2] D. A. Alcalá, J. A. Glick, and L. D. Carr, *Phys. Rev. Lett.* **118**, 210403 (2017).

- [3] J. Liu, S. C. Li, L. B. Fu, and D. F. Ye, *Nonlinear Adiabatic Evolution of Quantum Systems* (Springer, Singapore, 2018).  
 [4] S. Martínez-Garaot, G. Pettini, and M. Modugno, *Phys. Rev. A* **98**, 043624 (2018).

- [5] T. Schumm, S. Hofferberth, L. M. Andersson, S. Wildermuth, S. Groth, I. Bar-Joseph, J. Schmiedmayer, and P. Krüger, *Nat. Phys.* **1**, 57 (2005).
- [6] S. Hofferberth, I. Lesanovsky, T. Schumm, A. Imambekov, V. Gritsev, E. Demler, and J. Schmiedmayer, *Nat. Phys.* **4**, 489 (2008).
- [7] M. Gring, M. Kuhnert, T. Langen, T. Kitagawa, B. Rauer, M. Schreitl, I. Mazets, D. Adu Smith, E. Demler, and J. Schmiedmayer, *Science* **337**, 1318 (2012).
- [8] A. L. Gaunt, T. F. Schmidutz, I. Gotlibovych, R. P. Smith, and Z. Hadzibabic, *Phys. Rev. Lett.* **110**, 200406 (2013).
- [9] T. Berrada, S. van Frank, R. Bücker, T. Schumm, J.-F. Schaff, and J. Schmiedmayer, *Nat. Commun.* **4**, 2077 (2013).
- [10] T. Berrada, S. van Frank, R. Bücker, T. Schumm, J.-F. Schaff, J. Schmiedmayer, B. Julía-Díaz, and A. Polls, *Phys. Rev. A* **93**, 063620 (2016).
- [11] B. D. Josephson, *Phys. Lett.* **1**, 251 (1962).
- [12] S. Raghavan, A. Smerzi, S. Fantoni, and S. R. Shenoy, *Phys. Rev. A* **59**, 620 (1999).
- [13] S. K. Adhikari, *Sci. Rep.* **7**, 16045 (2017).
- [14] A. Smerzi, S. Fantoni, S. Giovanazzi, and S. R. Shenoy, *Phys. Rev. Lett.* **79**, 4950 (1997).
- [15] M. Albiez, R. Gati, J. Fölling, S. Hunsmann, M. Cristiani, and M. K. Oberthaler, *Phys. Rev. Lett.* **95**, 010402 (2005).
- [16] L. D. Landau, *Phys. Z. Sowjetunion* **2**, 46 (1932).
- [17] G. Zener, *Proc. R. Soc. London Ser. A* **137**, 696 (1932).
- [18] B. Wu and Q. Niu, *Phys. Rev. A* **61**, 023402 (2000).
- [19] J. Liu, L. Fu, B. Y. Ou, S. G. Chen, D. I. Choi, B. Wu, and Q. Niu, *Phys. Rev. A* **66**, 023404 (2002).
- [20] N. Rosen and C. Zener, *Phys. Rev.* **40**, 502 (1932).
- [21] D. F. Ye, L. B. Fu, and J. Liu, *Phys. Rev. A* **77**, 013402 (2008).
- [22] A. D. Cronin, J. Schmiedmayer, and D. E. Pritchard, *Rev. Mod. Phys.* **81**, 1051 (2009).
- [23] C. R. Ekstrom, J. Schmiedmayer, M. S. Chapman, T. D. Hammond, and D. E. Pritchard, *Phys. Rev. A* **51**, 3883 (1995).
- [24] D. S. Weiss, B. C. Young, and S. Chu, *Phys. Rev. Lett.* **70**, 2706 (1993).
- [25] A. Peters, K. Y. Chung, and S. Chu, *Nature (London)* **400**, 849 (1999).
- [26] M. R. Andrews, C. G. Townsend, H.-J. Miesner, D. S. Durfee, D. M. Kurn, and W. Ketterle, *Science* **275**, 637 (1997).
- [27] E. W. Hagley, L. Deng, M. Kozuma, M. Trippenbach, Y. B. Band, M. Edwards, M. Doery, P. S. Julienne, K. Helmerson, S. L. Rolston, and W. D. Phillips, *Phys. Rev. Lett.* **83**, 3112 (1999).
- [28] I. Bloch, T. W. Hänsch, and T. Esslinger, *Nature (London)* **403**, 166 (2000).
- [29] A. Perrin, R. Bücker, S. Manz, T. Betz, C. Koller, T. Plisson, T. Schumm, and J. Schmiedmayer, *Nat. Phys.* **8**, 195 (2012).
- [30] C. H. Lee, *Phys. Rev. Lett.* **97**, 150402 (2006).
- [31] Y.-J. Wang, D. Z. Anderson, V. M. Bright, E. A. Cornell, Q. Diot, T. Kishimoto, M. Prentiss, R. A. Saravanan, S. R. Segal, and S. Wu, *Phys. Rev. Lett.* **94**, 090405 (2005).
- [32] G. D. McDonald, H. Keal, P. A. Altin, J. E. Debs, S. Bennetts, C. C. N. Kuhn, K. S. Hardman, M. T. Johnsson, J. D. Close, and N. P. Robins, *Phys. Rev. A* **87**, 013632 (2013).
- [33] H. Müntinga, H. Ahlers, M. Krutzik, A. Wenzlawski, S. Arnold, D. Becker, K. Bongs, H. Dittus, H. Duncker, N. Gaaloul, C. Gherasim, E. Giese, C. Grzeschik, T. W. Hänsch, O. Hellmig, W. Herr, S. Herrmann, E. Kajari, S. Kleinert, C. Lämmerzahl, W. Lewoczko-Adamczyk, J. Malcolm, N. Meyer, R. Nolte, A. Peters, M. Popp, J. Reichel, A. Roura, J. Rudolph, M. Schiemangk, M. Schneider, S. T. Seidel, K. Sengstock, V. Tamma, T. Valenzuela, A. Vogel, R. Walser, T. Wendrich, P. Windpassinger, W. Zeller, T. van Zoest, W. Ertmer, W. P. Schleich, and E. M. Rasel, *Phys. Rev. Lett.* **110**, 093602 (2013).
- [34] Y. Shin, M. Saba, T. A. Pasquini, W. Ketterle, D. E. Pritchard, and A. E. Leanhardt, *Phys. Rev. Lett.* **92**, 050405 (2004).
- [35] G.-B. Jo, J.-H. Choi, C. A. Christensen, T. A. Pasquini, Y.-R. Lee, W. Ketterle, and D. E. Pritchard, *Phys. Rev. Lett.* **98**, 180401 (2007).
- [36] F. Baumgärtner, R. J. Sewell, S. Eriksson, I. Llorente-Garcia, J. Dingjan, J. P. Cotter, and E. A. Hinds, *Phys. Rev. Lett.* **105**, 243003 (2010).
- [37] Y. Torii, Y. Suzuki, M. Kozuma, T. Sugiura, T. Kuga, L. Deng, and E. W. Hagley, *Phys. Rev. A* **61**, 041602(R) (2000).
- [38] L. Pezzè, L. A. Collins, A. Smerzi, G. P. Berman, and A. R. Bishop, *Phys. Rev. A* **72**, 043612 (2005).
- [39] J. Grond, U. Hohenester, I. Mazets, and J. Schmiedmayer, *New J. Phys.* **12**, 065036 (2010).
- [40] J. Grond, U. Hohenester, J. Schmiedmayer, and A. Smerzi, *Phys. Rev. A* **84**, 023619 (2011).
- [41] N. F. Ramsey, *Phys. Rev.* **78**, 695 (1950).
- [42] S. Choi and B. Sundaram, *Phys. Rev. A* **77**, 053613 (2008).
- [43] S. C. Li, L. B. Fu, W. S. Duan, and J. Liu, *Phys. Rev. A* **78**, 063621 (2008).
- [44] S. C. Li, F. Q. Dou, and L. B. Fu, *Opt. Lett.* **42**, 3952 (2017).
- [45] L. B. Fu, D. F. Ye, C. Lee, W. Zhang, and J. Liu, *Phys. Rev. A* **80**, 013619 (2009).
- [46] E. C. G. Stueckelberg, *Helv. Phys. Acta* **5**, 369 (1932).
- [47] E. Majorana, *Nuovo Cimento* **9**, 43 (1932).
- [48] S. N. Shevchenko, S. Ashhab, and F. Nori, *Phys. Rep.* **492**, 1 (2010).
- [49] S. C. Li, L. B. Fu, and J. Liu, *Phys. Rev. A* **98**, 013601 (2018).
- [50] S. C. Li and L. B. Fu, *Phys. Rev. A* **101**, 023618 (2020).
- [51] G.-B. Jo, Y. Shin, S. Will, T. A. Pasquini, M. Saba, W. Ketterle, D. E. Pritchard, M. Vengalattore, and M. Prentiss, *Phys. Rev. Lett.* **98**, 030407 (2007).
- [52] M. Fattori, C. D'Errico, G. Roati, M. Zaccanti, M. Jona-Lasinio, M. Modugno, M. Inguscio, and G. Modugno, *Phys. Rev. Lett.* **100**, 080405 (2008).
- [53] M. Gustavsson, E. Haller, M. J. Mark, J. G. Danzl, G. Rojas-Kopeinig, and H.-C. Nägerl, *Phys. Rev. Lett.* **100**, 080404 (2008).
- [54] M. Kitagawa and M. Ueda, *Phys. Rev. A* **47**, 5138 (1993).
- [55] L. Pezzè, A. Smerzi, M. K. Oberthaler, R. Schmied, and P. Treutlein, *Rev. Mod. Phys.* **90**, 035005 (2018).
- [56] J. Estève, C. Gross, A. Weller, S. Giovanazzi, and M. K. Oberthaler, *Nature (London)* **455**, 1216 (2008).
- [57] C. Gross, T. Zibold, E. Nicklas, J. Estève, and M. K. Oberthaler, *Nature (London)* **464**, 1165 (2010).
- [58] M. F. Riedel, P. Böhi, Y. Li, T. W. Hänsch, A. Sinatra, and P. Treutlein, *Nature (London)* **464**, 1170 (2010).
- [59] C. Gross, H. Strobel, E. Nicklas, T. Zibold, N. Bar-Gill, G. Kurizki, and M. K. Oberthaler, *Nature (London)* **480**, 219 (2011).

- [60] B. Lücke, M. Scherer, J. Kruse, L. Pezzè, F. Deuretzbacher, P. Hyllus, O. Topic, J. Peise, W. Ertmer, J. Arlt, L. Santos, A. Smerzi, and C. Klempt, *Science* **334**, 773 (2011).
- [61] C. D. Hamley, C. S. Gerving, T. M. Hoang, E. M. Bookjans, and M. S. Chapman, *Nat. Phys.* **8**, 305 (2012).
- [62] G. Sorelli, M. Gessner, A. Smerzi, and L. Pezzè, *Phys. Rev. A* **99**, 022329 (2019).
- [63] B. Opanchuk, M. Egorov, S. Hoffmann, A. I. Sidorov, and P. D. Drummond, *Europhys. Lett.* **97**, 50003 (2012).
- [64] S. P. Nolan, Ph.D thesis, University of Queensland, 2018.
- [65] C. W. Gardiner, J. R. Anglin, and T. I. A. Fudge, [arXiv:cond-mat/0112129](https://arxiv.org/abs/cond-mat/0112129).
- [66] G. Spagnolli, G. Semeghini, L. Masi, G. Ferioli, A. Trenkwalder, S. Coop, M. Landini, L. Pezzè, G. Modugno, M. Inguscio, A. Smerzi, and M. Fattori, *Phys. Rev. Lett.* **118**, 230403 (2017).
- [67] B. V. Hall, S. Whitlock, R. Anderson, P. Hannaford, and A. I. Sidorov, *Phys. Rev. Lett.* **98**, 030402 (2007).
- [68] I. Lesanovsky, T. Schumm, S. Hofferberth, L. M. Andersson, P. Krüger, and J. Schmiedmayer, *Phys. Rev. A* **73**, 033619 (2006).
- [69] S. Hofferberth, I. Lesanovsky, B. Fischer, J. Verdu, and J. Schmiedmayer, *Nat. Phys.* **2**, 710 (2006).